CHEMISTRY OF MATERIALS

pubs.acs.org/cm

Article

Phase Evolution, Polymorphism, and Catalytic Activity of Nickel Dichalcogenide Nanocrystals

Marquix A. S. Adamson, Philip Yox, Thomas Hernandez, Fei Wang, and Javier Vela*

Cite This: Chem. Mater. 2022, 34, 746−755

Read Online

ACCESS | Metrics & More | Article Recommendations | Supporting Information

ABSTRACT: The nickel chalcogenide family contains multiple phases, each with varying properties that can be applied to an expansive range of industrially relevant processes. Specifically, pyrite-type NiS_2 and $NiSe_2$ have been used as electrocatalysts for oxygen or hydrogen evolution reactions. These pyrites have also been used in batteries and solar cells due to their optoelectronic and transport properties. The phase evolution of pyrite NiS_2 and polymorphism of $NiSe_2$ have briefly been studied in the literature, but there has been limited work focusing on the phase transformations within each of these two systems. Using experiments and calculations, we detail how pyrite NiS_2 nanocrystals decompose into hexagonal α-NiS, and how the synthesis of pyrite $NiSe_2$ nanocrystals is affected by the presence of two polymorphs, a metastable orthorhombic marcasite phase and a more stable cubic pyrite phase. Each reaction can be controlled by fine-tuning the reaction parameters, including temperature, time, and the precursor identity and concentration. Interestingly, both NiS_2 and $NiSe_2$ nanopyrites are active catalysts in the selective reduction of nitrobenzene to aniline, in agreement with other catalysts containing an fcc (sub) lattice. Our results demonstrate a feasible, logical process for synthesizing nanocrystalline pyrites without common byproducts or impurities. This work can help in solving a major problem suspected in preventing pyrite FeS_2 and similar materials from large-scale use: the presence of small amounts of secondary phases and impurities.

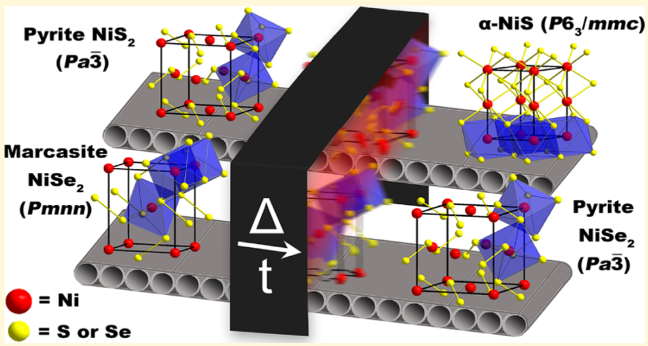

■ INTRODUCTION

Fool's gold—cubic FeS_2, also known as pyrite—is a readily available, biocompatible, and Earth-abundant semiconductor that has generated much interest in photovoltaics.[1] Unfortunately, the low open-circuit voltage of pyrite devices—widely believed to be caused by surface defects and marcasite impurities—has limited their application.[2−4] In addition to iron disulfide, the pyrite structure is adopted by a wide family of transition metal dichalcogenides, including those of nickel. Pyrite NiS_2 (p-NiS_2) is a small-band gap semiconductor,[5] while the two polymorphs of $NiSe_2$—pyrite (p-$NiSe_2$) and marcasite (m-$NiSe_2$)—are metallic.[6,7] The specific electronic character of nickel-based pyrites renders them useful as electrocatalysts for hydrogen evolution,[8−12] oxygen evolution,[8,12−14] and urea oxidation[8,13] reactions. Both p-NiS_2 and p-$NiSe_2$ have also been employed in batteries,[15,16] supercapacitors,[10,17,18] and dye-sensitized solar cells.[19,20] As with iron, several other nickel-based binary chalcogenide phases are known—including α-NiS, Ni_3S_2, Ni_3S_4, Ni_9S_8, hexagonal NiSe, and Ni_3Se_2—and their electronic properties range from semiconducting to metallic.[21−25] While multiple studies exist about their electrochemical, catalytic, and transport properties,[26−28] it is desirable to gain a deeper understanding of the transformations that occur between these different sulfide[29−31] and selenide binary phases and their polymorphs.[32−34]

The unit cells of three common 1:2 and 1:1 binary nickel chalcogenides—pyrite $NiCh_2$ (Ch = S, Se; $Pa\bar{3}$), marcasite $NiSe_2$ ($Pmnn$), and nickeline α-NiS ($P6_3/mmc$)—are shown in Figure 1. The nickel centers in all three phases are octahedrally coordinated. The pyrite structure is similar to the orthorhombic marcasite structure; however, the $[NiS_6]^{4-}$ octahedra are all corner-sharing in pyrite, whereas they are both corner- and edge-sharing in marcasite.[35,36] Importantly, while pyrite *versus* marcasite polymorphism is relatively well-studied among iron dichalcogenides,[37−40] less is known for nickel dichalcogenides.

Synthetically, nickel chalcogenides are most often prepared by solvothermal, hydrothermal, and sulfurization/selenization methods.[8,13,41,42] A few synthetic methods employ single-source precursor decomposition[43−45] or chemical vapor deposition.[12,46] Solution-phase preparations of pyrite nickel diselenide particles have been reported.[14,47,48] In this work, we

Received: October 14, 2021
Revised: December 21, 2021
Published: January 6, 2022

https://doi.org/10.1021/acs.chemmater.1c03557
Chem. Mater. 2022, 34, 746−755

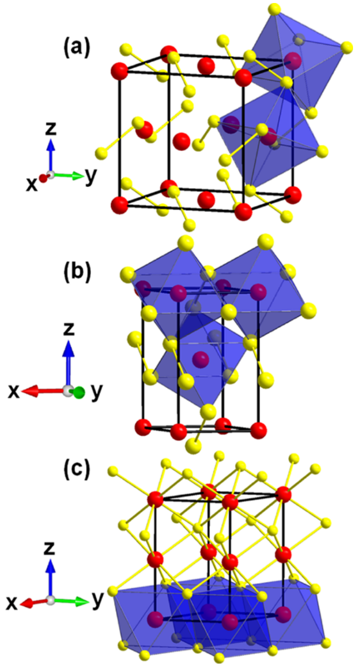

Figure 1. Unit cells of three common binary nickel chalcogenides: (a) pyrite (cubic, *Pa*$\bar{3}$), (b) marcasite (orthorhombic, *Pmnn*), and (c) nickeline (hexagonal, *P*6_3/*mmc*). Sample octahedra in blue are (a−c) corner-sharing, (b,c) edge-sharing, and (c) face-sharing.

use nickel disulfide and diselenide nanocrystals—synthesized colloidally—to elucidate the effect of different reaction parameters—precursors, temperature, and time—on the evolution of nanocrystalline *p*-NiS_2 *versus* α-NiS, as well as on the evolution of pyrite- *versus* marcasite-$NiSe_2$. Furthermore, we use computational methods to estimate the total energies of the two $NiSe_2$ polymorphs and use these calculations to explain our experimental observations. Finally, we demonstrate that both NiS_2 and $NiSe_2$ pyrites are active in the catalytic hydrogenation of nitrobenzene, with a selectivity toward the direct reduction product: aniline. A better understanding of the synthesis, polymorphism, and utility of nickel-based pyrites may broaden their appeal in multiple technological applications.

■ RESULTS AND DISCUSSION

Synthesis and Phase Evolution of *p*-NiS_2 Nanocrystals. Heating a mixture of nickel(II) acetate and sulfur in oleylamine (oleylNH_2) results in the formation of a crystalline material starting at *ca.* 100 °C (Scheme 1 and Table 1). X-ray diffraction (XRD) analysis of solids isolated by centrifugation from an aliquot of the reaction shows that the main crystalline product at or above 160 °C is pyrite nickel(II) disulfide nanocrystals (*p*-NiS_2) (Figures 2a and 3, see below). A second crystalline phase, made of hexagonal nickel(II) monosulfide nanocrystals, starts to form at 260 °C.[49] Interestingly, only the high-temperature alpha phase (α-NiS, nickeline) is observed as opposed to the lower temperature beta phase (β-NiS, millerite). The α−β transition is reported at 379 ± 3 °C,[50] and both phases have been synthesized independently.[51−53] However, in our experiments, we only observe α-NiS.

Transmission electron microscopy (TEM) measurements show that pyrite NiS_2 nanocrystals aggregate to form some flower- and rod-like motifs (Figure 4). The average *p*-NiS_2 particle size is 9.2 ± 1.6 nm, while the average aggregate size is

Scheme 1. Solution-Phase Synthesis and Mechanistic Possibilities for the Phase Evolution of Binary Nickel Sulfide Nanocrystals[a]

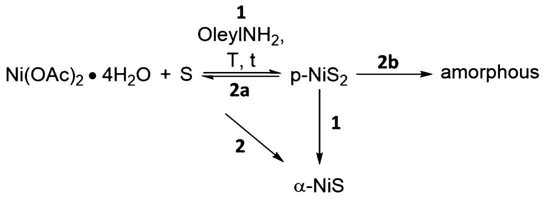

[a](**1**) α-NiS formation from an intermediate *p*-NiS_2 phase. (**2**) Direct α-NiS formation from molecular precursors (*p*-NiS_2 may decompose into different products **2a** or **2b**).

Table 1. Solution-Phase Synthesis of Nickel Chalcogenide Nanocrystals

precursors (M)				
Ni[a,b]	Ch[c]	*T* (°C)	*t* (min)	XRD products[d] (nm[e])
OAc	S	240	10	*p*-NiS_2 (9.5)
OAc	S	260	1	*p*-NiS_2 (10)
OAc	S	260	10	60% *p*-NiS_2 (13), α-NiS (20)
OAc	S	260	60	60% α-NiS (25), *p*-NiS_2 (12)
OAc	Se	200	1	78% *m*-$NiSe_2$ (27), *p*-$NiSe_2$ (15)
OAc	Se	260	1	55% *m*-$NiSe_2$, *p*-$NiSe_2$ (15)
OAc	Se	260	10	75% *p*-$NiSe_2$ (25), 15% *m*-$NiSe_2$, Se^0
OAc	Se	260	60	75% *p*-$NiSe_2$ (61), Se^0
OAc	Se (0.5)	260	60	97% *p*-$NiSe_2$ (34), *m*-$NiSe_2$
OAc	Se (0.25)	260	60	60% *p*-$NiSe_2$ (27), *m*-$NiSe_2$
St	Se (0.5)	260	60	*p*-$NiSe_2$ (26)
St	Se (0.5)	260	10	*p*-$NiSe_2$ (27)
St	Se (0.5)	260	1	*p*-$NiSe_2$ (32)
St	Se (0.5)	200	60	83% *p*-$NiSe_2$ (24), *m*-$NiSe_2$ (23)
St	Se (0.5)	200	10	77% *m*-$NiSe_2$ (33), *p*-$NiSe_2$ (16)

[a]OAc = Ni(acetate)$_2$·4H_2O, St = Ni(stearate)$_2$. [b]0.1 M in oleylamine. [c]1 M unless specified otherwise. [d]% given for main crystalline product(s), if applicable (sum = 100%). [e]Single crystalline domain (Scherrer) size calculated from XRD peak widths (see Methods).

69 ± 14 nm—see Supporting Information. Selected area electron diffraction (SAED) experiments of crystallites within these clusters accurately correspond to pyrite NiS_2. Analysis of the HRTEM and the corresponding fast Fourier transform (FFT) images further confirm the pyrite structure.

Repeating the aforementioned synthesis at 260 °C while varying the reaction time reveals further details about the relationship between *p*-NiS_2 and α-NiS nanophases (Figure 2b). *p*-NiS_2 forms rapidly—within 1 min of reaction—but its XRD reflections gradually decrease as the α-NiS reflections increase in intensity. After 10 min of reaction, *p*-NiS_2 and α-NiS become *ca.* 60 and 40% of the crystalline sample, respectively (Figure 3). This strongly suggests that either the *p*-NiS_2 phase transforms into the α-NiS phase over time (path 1 in Scheme 1) or that leftover (unreacted) precursors slowly react to form the secondary α-NiS byproduct while *p*-NiS_2 slowly decomposes into an amorphous material (path 2 in Scheme 1). In support of the first of these mechanistic hypotheses, powder XRD analysis shows that annealing *p*-NiS_2 nanocrystals at 600 °C results in the formation of phase-pure α-NiS (Figure 2c).

To learn more about this annealing process, we studied the transformation of *p*-NiS_2 into α-NiS by thermal analysis

https://doi.org/10.1021/acs.chemmater.1c03557
Chem. Mater. 2022, 34, 746−755

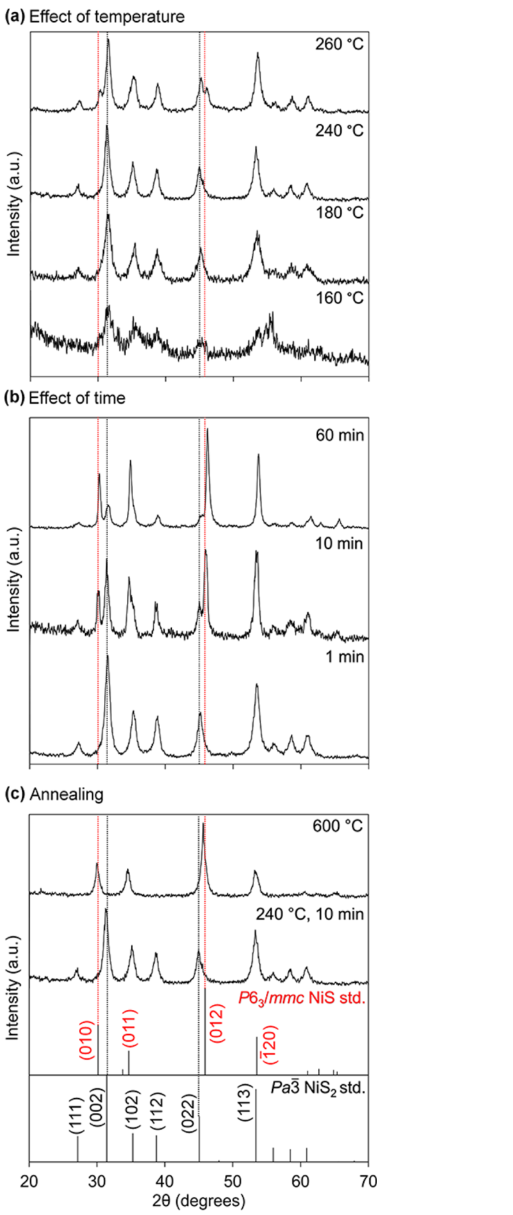

Figure 2. Powder XRD patterns of nickel sulfide nanocrystals synthesized in oleylamine at different temperatures after 10 min of reaction (a), reaction times at 260 °C (b), and after solid annealing at 600 °C (c) [0.1 M Ni(acetate)$_2$·4H$_2$O, 1 M S, see Scheme 1 and Methods]. Dashed guidelines for key reflections from nickeline NiS (ICSD 29313) and pyrite NiS$_2$ (ICSD 79670) are included for clarity.[49]

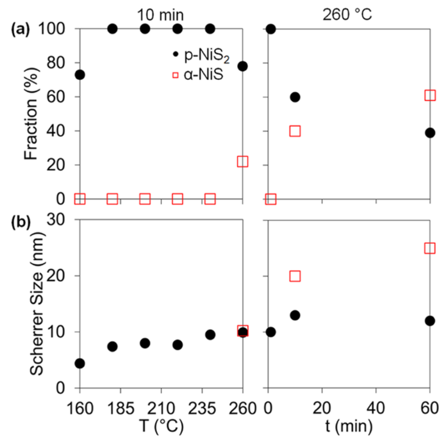

Figure 3. Percentage of crystalline products (a) and average Scherrer size (b) for p-NiS$_2$ and α-NiS nanocrystals synthesized in oleylamine under different conditions [0.1 M Ni(acetate)$_2$·4H$_2$O, 1 M S, see Methods]. In all panels, individual data points are from aliquots, except the last data point in each panel, which was cooled naturally.

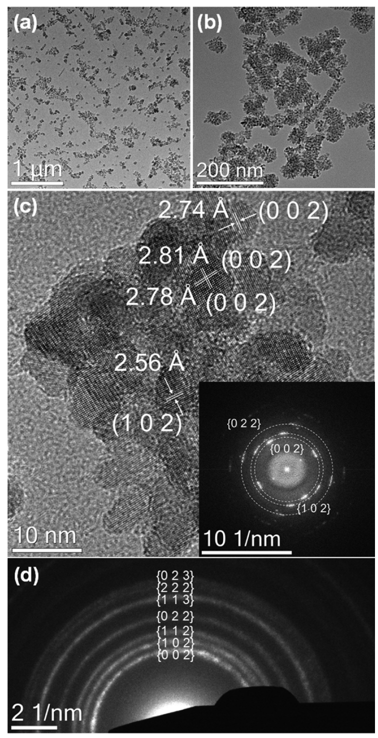

Figure 4. Representative TEM (a,b), HR TEM [(c), FFT inset], and SAED (d) measurements of p-NiS$_2$ nanocrystals synthesized from Ni(acetate)$_2$·4H$_2$O (0.1 M) and S (1 M) in oleylamine at 240 °C for 10 min (see Methods). The (1 1 1) plane is absent in this example, and although the (0 2 2) plane is difficult to distinguish in HRTEM due to plane overlap, the FFT confirms its presence.

(Figure 5). An exothermic peak in the differential scanning calorimetry (DSC) curve at 296 °C corresponds to the decomposition of p-NiS$_2$. This transition begins at *ca.* 260 °C, the point at which α-NiS starts to crystallize in solution (see above). The thermogravimetric analysis (TGA) curve first levels off at about 74% of the original mass, close to the theoretical value for the extrusion of one [S] equivalent from p-NiS$_2$ (Scheme 2). A second endothermic peak in the DSC at 450−470 °C is consistent with the evaporation of elemental sulfur. This causes a change in the slope of the TGA curve due to additional mass loss as sulfur gas leaves the system. Analysis of peak widths observed by powder XRD shows single-crystalline domain (Scherrer) sizes for p-NiS$_2$ and α-NiS nanocrystals before and after annealing of 9.5 and 12 nm, respectively. Similar thermal studies for pyrite FeS$_2$ also show the decomposition to the sulfur-deficient phase (pyrrhotite, Fe$_{1-x}$S) at around the same temperature.[54,55]

Using available thermodynamic data, a back-of-the-envelope calculation reveals that the extrusion of S from p-NiS$_2$ is disfavored by enthalpy ($\Delta H°_r$ = +43.5 kJ/mol) but favored by entropy ($\Delta S°_r$ = +13.1 J/mol·K)—that is, both are positive (>0). Assuming these remain relatively constant, we calculate that the overall free energy change for the reaction ($\Delta G°_r$) is positive throughout our solution phase experiments and even

https://doi.org/10.1021/acs.chemmater.1c03557
Chem. Mater. 2022, 34, 746−755

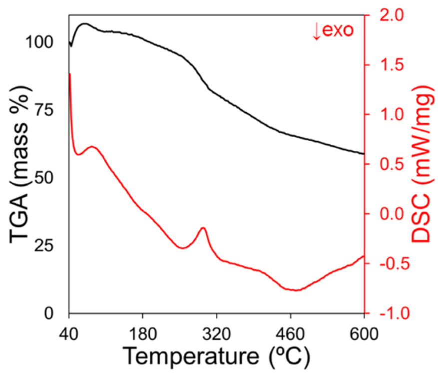

Figure 5. Thermal analysis of *p*-NiS_2 nanocrystals.

Scheme 2. Decomposition of *p*-NiS_2

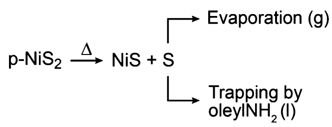

all the way up past the aforementioned solid annealing temperature of 600 °C—in other words, the reaction remains endothermic and is not spontaneous (see Supporting Information, Scheme 2). We reconcile our observations with these calculations as follows: (1) in solution, the sulfur released must be undergoing a secondary reaction, driving the overall decomposition of *p*-NiS_2. A likely culprit is oleylamine, present in excess, as it is known to form thioamides and other products upon heating with sulfur (see Supporting Information).[56,57] (2) In the solid state, sulfur escapes the system as a vapor (see above).

Scheme 3. Solution-Phase Synthesis and Mechanistic Possibilities for the Formation of Nanocrystalline Nickel Diselenide Polymorphs[a]

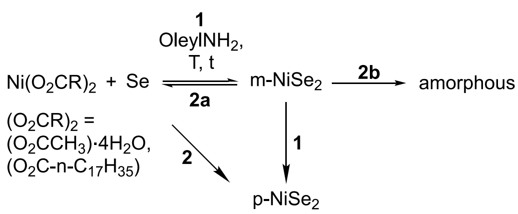

[a](1) *p*-$NiSe_2$ formation from an intermediate *m*-$NiSe_2$ phase. (2) Direct *p*-$NiSe_2$ formation from molecular precursors (*m*-$NiSe_2$ may decompose into different products **2a** or **2b**).

Synthesis and Phase Evolution of $NiSe_2$ Nanocrystals. The reaction of nickel(II) carboxylates with elemental selenium in oleylamine results in the formation of nanocrystalline $NiSe_2$ polymorphs (Scheme 3 and Table 1). Powder XRD analysis of solids isolated after only 1 min of reaction at 260 °C shows reflections corresponding to the cubic pyrite phase of $NiSe_2$ (Figures 6 and 7). This is initially accompanied by reflections from a minor byproduct corresponding to the orthorhombic marcasite polymorph of $NiSe_2$. Longer reaction times and higher synthetic temperatures result in the disappearance of the latter marcasite phase, although an excess of elemental selenium (Se^0) becomes apparent in some cases (see below).

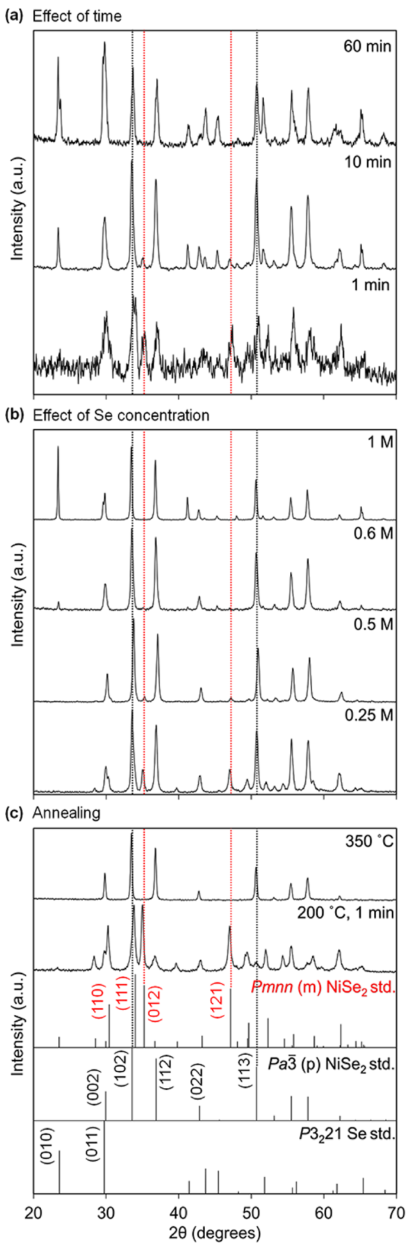

Figure 6. Powder XRD patterns of nickel diselenide nanocrystals synthesized in oleylamine at different reaction times with 1 M Se at 260 °C (a), Se precursor concentrations at 260 °C for 1 h (b), and after solid annealing at 350 °C (c) [0.1 M Ni(acetate)$_2$·4H_2O, see Scheme 3 and Methods]. Dashed guidelines for key reflections from *m*-$NiSe_2$ (ICSD 5071) and *p*-$NiSe_2$ (ICSD 40330) are included for clarity. Trigonal Se^0 (ICSD 9008579).[49]

Based on these observations, we propose two possible mechanisms for the formation of $NiSe_2$ nanocrystals. In one of these mechanisms, the precursors first nucleate *m*-$NiSe_2$ seeds, which then phase transform into *p*-$NiSe_2$ over time (path 1 in Scheme 3). In support of this possibility, thermal analysis and powder XRD show that annealing a solid *ca.* 1:1 mixture of both polymorphs at or above 350 °C results in the formation of phase-pure *p*-$NiSe_2$ without a significant loss in the sample mass (Figures 6c and Supporting Information). In a second mechanism, both *p*-$NiSe_2$ and *m*-$NiSe_2$ concomitantly form from the precursors (path 2 in Scheme 3), but only the pyrite phase accumulates over time (see below). In support of both

https://doi.org/10.1021/acs.chemmater.1c03557
Chem. Mater. 2022, 34, 746−755

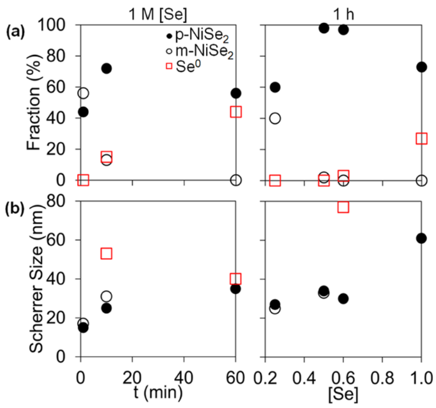

Figure 7. Percentage of crystalline products (a) and average Scherrer size (b) for nickel diselenide nanocrystals synthesized in oleylamine under different conditions [0.1 M Ni(acetate)$_2$·4H$_2$O, 260 °C, see Scheme 3, Figure 6, and Methods]. Left panel data from aliquots, except 60 min, which was cooled naturally. Right panel data are all after natural cooling.

paths 1 and 2, computations show the pyrite phase to be more stable than the marcasite phase (see below).

To further understand this process, we studied how the initial concentration of selenium affects the formation of nanocrystalline $NiSe_2$. For a given set of experimental conditions, low initial [Se] concentrations produce a mixture of pyrite- and marcasite-$NiSe_2$ (Figure 6b). In contrast, high initial [Se] concentrations suppress the formation of marcasite; however, too much selenium can be a nuisance as it is difficult to remove at the end of the reaction. Using 0.1 M [Ni] and at 260 °C for 1 h, a convenient middle point is about 0.5 M [Se] (Figures 6b and 7). Because both pyrite- and marcasite-$NiSe_2$ have the same stoichiometry, we hypothesize that the effect of higher selenium concentrations may be to speed up the rate of nucleation of *p*-$NiSe_2$ relative to *m*-$NiSe_2$ (path 2 in Scheme 3). Additionally—or alternatively—it is possible that higher selenium concentrations may speed up the phase transformation from marcasite to pyrite in this system (second step of path 1 in Scheme 3). Interestingly, support for the latter of these two hypotheses can be found in the iron pyrite literature, where higher partial pressures of sulfur—of H_2S—gas facilitated the phase transformation from *m*-FeS_2 to *p*-FeS_2.[55,58,59]

TEM shows that *p*-$NiSe_2$ nanocrystals prepared from nickel(II) acetate are significantly aggregated (see Supporting Information). Using nickel(II) stearate, a precursor with a longer carboxylate chain, helps provide better control over particle size and narrower polydispersity (Figure 8). We hypothesize that the increased steric hindrance afforded by the larger stearate ligand slows down the kinetics of precursor decomposition and/or nanocrystal growth. The increased sterics of surface-bound stearate ligands may also help in better passivating the nanocrystal, preventing it from aggregating into larger clusters. Furthermore, we find that using nickel(II) stearate at 260 °C eliminates any trace of *m*-$NiSe_2$ or Se^0 impurities. A time-dependent experiment at this temperature shows that the particle size is determined very early on, reaching between 25 and 30 nm within 1 min from the start of the reaction (see Supporting Information). In all cases, HRTEM and FFT analyses confirm the pyrite structure of the *p*-$NiSe_2$ nanocrystals.

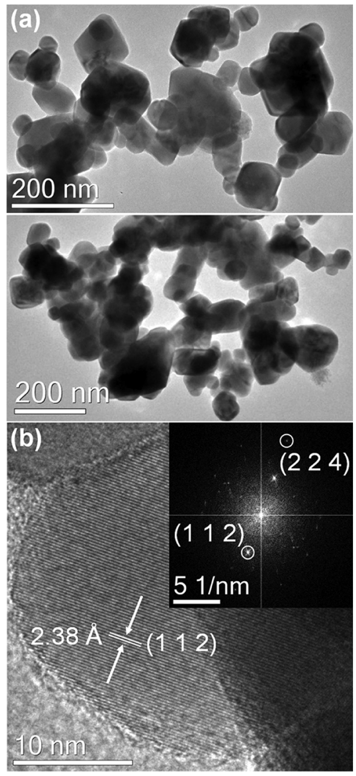

Figure 8. Representative TEM (a), HR TEM (b), and FFT (inset) of *p*-$NiSe_2$ nanocrystals synthesized from Ni(stearate)$_2$ (0.1 M) and Se (0.5 M) in oleylamine at 260 °C for 60 min (see Methods).

Dichalcogenide Polymorphism from Calculations. To better understand the phase evolution of the two $NiSe_2$ polymorphs, we performed density functional theory calculations (Table 2, Figure 9, see Supporting Information). Both local density approximation (LDA) and Perdew−Burke−Ernzerhof (PBE) functionals yield total *p*-$NiSe_2$ and *m*-$NiSe_2$ energies that are separated by less than 35 meV per formula unit (f.u.). (We note that these calculations lack surface energy differentials or what effect they may have on the bulk free energies.[60]) The pyrite unit cell volume calculated with LDA (192.997 Å^3) and PBE (209.683 Å^3) is, respectively, 9 and 2% smaller than that reported in the ICSD (212.018 Å^3).[49] The Ni−Se bond distances calculated using LDA and PBE are both within 4% of those reported for pyrite (2.488 Å) and marcasite (2.43 and 2.45 Å) (Table 2). However, the *p*-$NiSe_2$ Se−Se bond distances of 2.56 Å for LDA and 2.53 Å for PBE are longer than those reported of 2.42 Å. Critically, LDA predicts the cubic pyrite phase to be 32.9 meV lower in energy compared to the orthorhombic marcasite phase, while PBE predicts the opposite (Figure 9). This discrepancy stems from the functionals' different approximations to electronic exchange−correlation energy.

To arbitrate the contradiction between LDA and PBE, we applied the PBEsol functional, which uses a generalized gradient approximation (GGA) to better describe solids containing 3d metals.[61,62] In agreement with LDA, PBEsol predicts pyrite $NiSe_2$ to be more stable than marcasite-$NiSe_2$. To avoid Pulay stress[63]—an artificial isotropic stress that results from an incomplete basis set—we performed structural optimization using volume scans. Atomic positions and cell shapes were optimized at a series of fixed unit cell volumes, and

https://doi.org/10.1021/acs.chemmater.1c03557
Chem. Mater. 2022, 34, 746−755

Table 2. Assessing $NiSe_2$ Polymorphism from Calculations[a]

Method	Pyrite ($Pa\bar{3}$)	Marcasite ($Pmnn$)
LDA	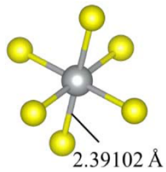 2.39102 Å	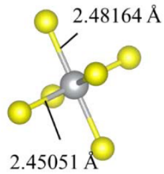 2.48164 Å; 2.45051 Å
V (Å^3/f.u.)	48.25	50.54
E (eV)	-15.8968	-15.8639
PBEsol[b]	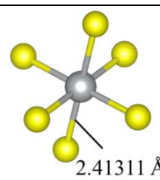 2.41311 Å	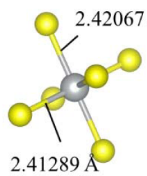 2.42067 Å; 2.41289 Å
V_{eq} (Å^3/f.u.)	49.539(3)	51.825(2)
$E_{tot,min}$ Fitted (eV)	−14.76114(1)	−14.73492(6)
$E_{tot,min}$ VASP (eV)	−14.76117(3)	−14.73498(5)

[a]Total energy calculations using a 20 × 20 × 20 k-point mesh optimizing cell volume, cell shape, and atomic position. [b]Values from minima of volume scans using PBEsol.

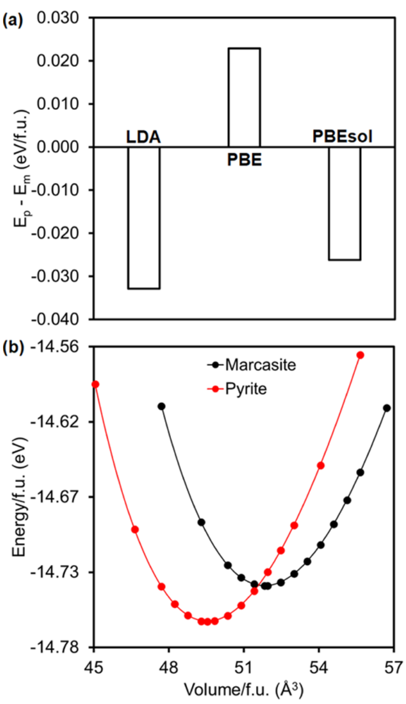

Figure 9. Calculated relative energies (a) and energy-volume curves [from PBEsol, using Birch−Murnaghan equation of state fitting, (b)] of pyrite and marcasite polymorphs of $NiSe_2$.

energy−volume (E−V) data were fitted with the Birch−Murnaghan equation of state.[64,65]

The minima of these E−V curves pinpoint the equilibrium volumes (V_{eq}, Table 2) and total energies ($E_{tot,min}$ Fitted, Table 2) of the two structure types at zero external pressure (Figure 9b). The predicted unit cell volume for p-$NiSe_2$ is 198.16 Å^3, only 6% smaller than the experimental value. To validate this approach, the total energy at V_{eq} was calculated with VASP ($E_{tot,min}$ VASP, Table 2), and this was virtually equal to $E_{tot,min}$ Fitted using the Birch−Murnaghan equation of state fitting. Based on its lower $E_{tot,min}$, pyrite is predicted to be the more stable phase and marcasite to be metastable, in agreement with our experiments. We note that the accuracy of exchange correlation functionals was rigorously investigated for iron disulfides, but nickel disulfides remained relatively understudied.[66−68]

Nickel Dichalcogenides as Catalysts. The reduction of nitroarenes is an industrially useful reaction that is often catalyzed by metallic and related nanoparticles.[69] Based on previous reports on the use of pyrite-type NiS_2 and $NiSe_2$ as electrocatalysts,[8,13] we wondered whether these materials could serve as catalysts for the solution-phase hydrogenation of nitrobenzene. Recently, we showed that this deceivingly simple reaction can produce highly divergent results: while some catalysts yield aniline, others lead to condensation products such as azoxyarene and azobenzene (see Supporting Information). An empirical parameter that appears to correlate with this preference is the presence of a face-centered cubic (fcc) lattice. Many monometallic and alloyed nanoparticles—and a nanoparticulate intermetallic (Pd_3Pb)—containing an fcc structure are selective to aniline. In contrast, nanoparticles of multiple other atomically precise intermetallics containing a different structure type are selective to azoxyarene and azobenzene.[70]

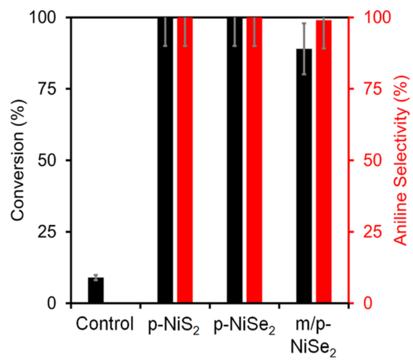

Figure 10. Catalytic reduction of $PhNO_2$ in the absence of a catalyst (control) *versus* in the presence of nickel dichalcogenide nanoparticles (50 μM $PhNO_2$ in 2 mL of ethanol, 10 mg catalyst, 21 °C, 4 h, see Methods).

Scheme 4. Catalytic Reduction of Nitrobenzene

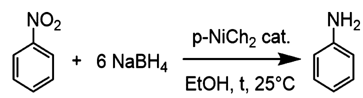

To probe this possibility, we tested pyrite NiS_2 and $NiSe_2$ nanocrystals as catalysts for the solution-phase hydrogenation of nitrobenzene ($PhNO_2$) (Scheme 4, see Methods). Under ambient conditions, gas chromatography−mass spectroscopy (GCMS) analysis shows that nitrobenzene is fully reduced with either catalyst within only 4 h of reaction (Figure 10, Table 3). Furthermore, both pyrite nanocatalysts show complete (100%) selectivity for aniline ($PhNH_2$). This result is in perfect agreement with what we could have predicted based on our aforementioned observation, as both pyrite

https://doi.org/10.1021/acs.chemmater.1c03557
Chem. Mater. 2022, 34, 746−755

Table 3. Catalytic Nitrobenzene Reduction with Nanocrystalline Nickel Dichalcogenides[a]

catalyst	t (h)	conv. (%)[b]	aniline sel. (%)[b]
none (control)	4	9	0
p-NiS_2	4	100	100
p-$NiSe_2$	4	100	100
m/p-$NiSe_2$ (1:1)	4	89	99

[a]50 μM $PhNO_2$ in 2 mL of ethanol, 10 mg catalyst, 21 °C (see Methods). [b]Max. error ± 10%.

materials contain an fcc sublattice of nickel(II) centers, with dichalcogenides (S_2^{2-} or Se_2^{2-}) filling in the octahedral holes (Figure 1a). Therefore, not only fcc-structured catalysts may be selective to aniline but also those containing an fcc sublattice within their structure. The speed, ease, and high selectivity of these reactions provide a positive contrast with other reported catalysts and conditions which, in some cases, result in incomplete conversion or have limited selectivities.[70] Interestingly, when a *ca.* 1:1 mixture of m- and p-$NiSe_2$ is used, conversion is only 89%, indicating that the presence of marcasite impurities can be detrimental to catalysis.

CONCLUSIONS

To summarize, we describe the rich and facile phase evolution chemistry of pyrite NiS_2 and $NiSe_2$ nanocrystals synthesized from solution. Upon heating, pyrite NiS_2 transforms into hexagonal α-NiS, while marcasite $NiSe_2$ transforms into pyrite $NiSe_2$. Simple thermodynamics calculations show that the decomposition of p-NiS_2 into α-NiS is an endergonic, thermodynamically unfavorable process with a positive ΔG_r° (>0). Therefore, to explain its decomposition, it is necessary to think about how the extruded sulfur is being either trapped in solution—by reaction with excess oleylamine solvent—or lost from the system in the solid state—by evaporation upon heating.

Additionally, we show that the synthesis of pyrite $NiSe_2$ nanocrystals is often accompanied by a polymorphic marcasite $NiSe_2$ impurity. Calculations using LDA and PBEsol functionals accurately predict pyrite to be the more stable form of $NiSe_2$. This is consistent with our experimental findings showing that marcasite transforms into pyrite $NiSe_2$ over time. Interestingly, we find that both pyrite NiS_2 and $NiSe_2$ are active catalysts in the reduction of nitrobenzene. Both materials display high selectivity for aniline, in agreement with other catalysts for this transformation containing an fcc (sub) lattice. This work provides a mechanistic rationale for the selective synthesis of pyrite phase nickel dichalcogenides, the energetics of their decomposition and phase transformations, and their potential utility in catalysis. We expect this work will be extended to other stable and metastable transition metal pyrites in other industrially relevant applications. In particular, we anticipate that this work might help cure the degradation of FeS_2 devices due to the rapid formation of sulfur-deficient phases or polymorphic byproducts that may be present in the early stages of synthesis or device fabrication.

METHODS

Materials. Sulfur (99.5%) was purchased from Fisher Scientific; nickel(II) acetate tetrahydrate (98%), oleylamine (oleylNH_2, technical grade, 70%), and selenium (100 mesh, 99.99%) from Aldrich; nickel(II) stearate from STREM; nitrobenzene (99%) from Oakwood Chemical; ethanol (EtOH) from Decon Labs; and sodium borohydride ($NaBH_4$, powder, 98+%) from Acros Organics.

Synthesis. *NiS_2 nanocrystals* were synthesized by a slightly modified literature procedure.[71] In a typical synthesis, nickel(II) acetate tetrahydrate (1 mmol, 0.2488 g), elemental sulfur (10 mmol, 0.3207 g), and oleylamine (10 mL) were mixed together in a three-neck flask until the two solids dissolved (~1 h). While stirring, the mixture was heated to ~90 °C and degassed under dynamic vacuum for ≤15 min. The flask was refilled with N_2 and heated to the desired time and temperature (see above). *$NiSe_2$ nanocrystals* were synthesized by mixing together the nickel(II) carboxylate precursor [0.5 mmol, 0.1244 g Ni(acetate)$_2$·4H_2O or 0.3128 g Ni(stearate)$_2$], elemental selenium (1 mmol, 0.0789 g or 2.5 mmol, 0.1974 g), and oleylamine (10 or 5 mL) in a three-neck flask. While stirring, the mixture was heated to ~90 °C and degassed under dynamic vacuum for 1 h. The flask was refilled with N_2 and heated to the desired time and temperature (see above). *Purification*: The crude solution was suspended in 5 mL of chloroform in a centrifuge tube. An excess amount of ethanol was added, and the tube was centrifuged at 4500 rpm for 5 min. After removing the supernatant, the process was repeated three times. *Annealing*: NiS_2 nanocrystals were annealed by adding 20 mg of the dried powder to an alumina crucible and heating to 600 °C under Ar flow in a TGA−DSC instrument. $NiSe_2$ nanocrystals were annealed by heating dried powders to 350 °C under N_2 flow in a tube furnace for 40 min.

Structural Characterization. Powder XRD patterns were collected using Cu Kα radiation on a Rigaku Ultima IV (40 kV, 44 mA) diffractometer using a background-less quartz sample holder. Scherrer analysis was performed with Jade using a κ value of 0.9. TEM and SAED were performed on a FEI Tecnai G2-F20. Size distributions contain at least 300 particles. *Other*: TGA and DSC data were collected using a NETZSCH STA 449 F1 at a rate of 10 °C/min.

Catalysis. Nitrobenzene (0.1 mmol, 10 μL) and ethanol (2 mL) were added to a 5 mL vial. The catalyst (10 mg of purified p-NiS_2 or p-$NiSe_2$ nanocrystals) was subsequently added. Phase-pure p-NiS_2 was synthesized at 240 °C for 10 min (see above), phase-pure p-$NiSe_2$ was prepared from Ni(stearate)$_2$ at 260 °C for 10 min, and a 1:1 mixture of m/p-$NiSe_2$ was prepared from Ni(acetate)$_2$ at 200 °C for 1 h. While stirring at 300 rpm, $NaBH_4$ (23 mg, 0.6 mmol) was added at room temperature (21 °C), and stirring was continued for 4 h. Aliquots (0.5 mL) were filtered using a 0.2 μm PTFE filter. A portion of the filtered aliquots was consistently diluted and analyzed using GCMS. Control experiments in the absence of a catalyst show only residual nitrobenzene reduction over 4 h.

First-Principles Total Energy Calculations. The Vienna Ab initio Software Package (VASP)[72−75] was used to compare the relative stability between the marcasite- and the pyrite-type structures for $NiSe_2$. The pseudopotentials generated with the projector augmented wave method[76] were used for both Ni and Se. The electronic exchange−correlation was treated with local density approximation (LDA), Perdew−Burke−Ernzerhof and modified PBE (PBEsol)[61,62] functionals. The energy cutoff for the plane wave basis functions was 269.5 eV. The energy convergence criterion was 1×10^{-4} eV for the self-consistent electronic iterations. For structural optimizations, we tried both full structural optimizations and volume scans. The first Brillouin zones were sampled with Monkhorst meshes,[77] at least $7 \times 7 \times 7$ for the pyrite structure and $11 \times 9 \times 7$ for the marcasite structure in volume scans, and $20 \times 20 \times 20$ for both structures in full structural optimization. In full optimization, the atomic coordinates, cell volume, and cell shape were all allowed to relax simultaneously. For volume scans, atomic positions and unit cell shapes were optimized at a series of fixed unit cell volumes. All optimizations employ the conjugate gradient algorithm.[78] The total energy *versus* unit cell volume data from volume scans were fitted with the Birch−Murnaghan equation of state to determine the equilibrium volumes and total energy minima.[64,65]

ASSOCIATED CONTENT

Supporting Information

The Supporting Information is available free of charge at https://pubs.acs.org/doi/10.1021/acs.chemmater.1c03557.

Particle size histogram for p-NiS_2, thermodynamic calculations for the decomposition of p-NiS_2, proposed sulfur trapping mechanism, mixed-phase $NiSe_2$ TGA-DSC, TEM of p-$NiSe_2$ particles made from nickel(II) acetate, powder XRD of $NiSe_2$ made from nickel(II) stearate, computational data for PBEsol, PBE volume scans, $NiSe_2$ computational data table, and nitroarene reduction pathway scheme (PDF)

AUTHOR INFORMATION

Corresponding Author

Javier Vela − *Department of Chemistry, Iowa State University, Ames, Iowa 50011, United States; Ames Laboratory, Ames, Iowa 50011, United States;* orcid.org/0000-0001-5124-6893; Email: vela@iastate.edu

Authors

Marquix A. S. Adamson − *Department of Chemistry, Iowa State University, Ames, Iowa 50011, United States*

Philip Yox − *Department of Chemistry, Iowa State University, Ames, Iowa 50011, United States; Ames Laboratory, Ames, Iowa 50011, United States;* orcid.org/0000-0002-8524-8202

Thomas Hernandez − *Department of Chemistry, Iowa State University, Ames, Iowa 50011, United States*

Fei Wang − *Department of Chemistry, Missouri State University, Springfield, Missouri 65897, United States;* orcid.org/0000-0001-6957-1360

Complete contact information is available at: https://pubs.acs.org/10.1021/acs.chemmater.1c03557

Notes

The authors declare no competing financial interest.

ACKNOWLEDGMENTS

J.V. gratefully acknowledges the U.S. National Science Foundation for a grant from the Division of Chemistry, Macromolecular, Supramolecular, and Nanochemistry Program (1905066). The authors thank Carena L. Daniels and Kamel Harrata for assistance with catalysis experiments.

REFERENCES

(1) Wadia, C.; Alivisatos, A. P.; Kammen, D. M. "Materials Availability Expands the Opportunity for Large-Scale Photovoltaics Deployment". *Environ. Sci. Technol.* **2009**, *43*, 2072−2077.

(2) Sun, R.; Chan, M. K. Y.; Ceder, G. "First-Principles Electronic Structure and Relative Stability of Pyrite and Marcasite: Implications for Photovoltaic Performance". *Phys. Rev. B: Condens. Matter Mater. Phys.* **2011**, *83*, 235311.

(3) Steinhagen, C.; Harvey, T. B.; Stolle, C. J.; Harris, J.; Korgel, B. A. "Pyrite Nanocrystal Solar Cells: Promising, or Fool's Gold?". *J. Phys. Chem. Lett.* **2012**, *3*, 2352−2356.

(4) Rahman, M.; Boschloo, G.; Hagfeldt, A.; Edvinsson, T. "On the Mechanistic Understanding of Photovoltage Loss in Iron Pyrite Solar Cells". *Adv. Mater.* **2020**, *32*, 1905653.

(5) Jourshabani, M.; Shariatinia, Z.; Achari, G.; Langford, C. H.; Badiei, A. "Facile Synthesis of NiS_2 Nanoparticles Ingrained in a Sulfur-Doped Carbon Nitride Framework with Enhanced Visible Light Photocatalytic Activity: Two Functional Roles of Thiourea". *J. Mater. Chem. A* **2018**, *6*, 13448−13466.

(6) Zhou, J.; Yuan, L.; Wang, J.; Song, L.; You, Y.; Zhou, R.; Zhang, J.; Xu, J. "Combinational Modulations of $NiSe_2$ Nanodendrites by Phase Engineering and Iron-Doping Towards an Efficient Oxygen Evolution Reaction". *J. Mater. Chem. A* **2020**, *8*, 8113−8120.

(7) Schuster, C.; Gatti, M.; Rubio, A. "Electronic and Magnetic Properties of NiS_2, NiSSe, and $NiSe_2$ by a Combination of Theoretical Methods". *Eur. Phys. J. B* **2012**, *85*, 325.

(8) Liu, H.; Liu, Z.; Wang, F.; Feng, L. "Efficient Catalysis of N-Doped NiS/NiS_2 Heterogeneous Structure". *Chem. Eng. J.* **2020**, *397*, 125507.

(9) Tian, T.; Huang, L.; Ai, L.; Jiang, J. "Surface Anion-Rich NiS_2 Hollow Microspheres Derived from Metal−Organic Frameworks as a Robust Electrocatalyst for the Hydrogen Evolution Reaction". *J. Mater. Chem. A* **2017**, *5*, 20985−20992.

(10) Pang, H.; Wei, C.; Li, X.; Li, G.; Ma, Y.; Li, S.; Chen, J.; Zhang, J. "Microwave-Assisted Synthesis of NiS_2 Nanostructures for Supercapacitors and Cocatalytic Enhancing Photocatalytic H_2 Production". *Sci. Rep.* **2014**, *4*, 3577.

(11) Yu, B.; Wang, X.; Qi, F.; Zheng, B.; He, J.; Lin, J.; Zhang, W.; Li, Y.; Chen, Y. "Self-Assembled Coral-like Hierarchical Architecture Constructed by $NiSe_2$ Nanocrystals with Comparable Hydrogen-Evolution Performance of Precious Platinum Catalyst". *ACS Appl. Mater. Interfaces* **2017**, *9*, 7154−7159.

(12) Lee, S.; Cha, S.; Myung, Y.; Park, K.; Kwak, I. H.; Kwon, I. S.; Seo, J.; Lim, S. A.; Cha, E. H.; Park, J. "Orthorhombic $NiSe_2$ Nanocrystals on Si Nanowires for Efficient Photoelectrochemical Water Splitting". *ACS Appl. Mater. Interfaces* **2018**, *10*, 33198−33204.

(13) Liu, Z.; Zhang, C.; Liu, H.; Feng, L. "Efficient Synergism of $NiSe_2$ Nanoparticle/NiO Nanosheet for Energy-Relevant Water and Urea Electrocatalysis". *Appl. Catal., B* **2020**, *276*, 119165.

(14) Du, Y.; Cheng, G.; Luo, W. "$NiSe_2$/$FeSe_2$ Nanodendrites: A Highly Efficient Electrocatalyst for Oxygen Evolution Reaction". *Catal. Sci. Technol.* **2017**, *7*, 4604−4608.

(15) Sun, R.; Liu, S.; Wei, Q.; Sheng, J.; Zhu, S.; An, Q.; Mai, L. "Mesoporous NiS_2 Nanospheres Anode with Pseudocapacitance for High-Rate and Long-Life Sodium-Ion Battery". *Small* **2017**, *13*, 1701744.

(16) Xue, M.-Z.; Fu, Z.-W. "Lithium Electrochemistry of $NiSe_2$: A New Kind of Storage Energy Material". *Electrochem. Commun.* **2006**, *8*, 1855−1862.

(17) Dai, Z.; Zang, X.; Yang, J.; Sun, C.; Si, W.; Huang, W.; Dong, X. "Template Synthesis of Shape-Tailorable NiS_2 Hollow Prisms as High-Performance Supercapacitor Materials". *ACS Appl. Mater. Interfaces* **2015**, *7*, 25396−25401.

(18) Wang, S.; Li, W.; Xin, L.; Wu, M.; Long, Y.; Huang, H.; Lou, X. "Facile Synthesis of Truncated Cube-like $NiSe_2$ Single Crystals for High Performance Asymmetric Supercapacitors". *Chem. Eng. J.* **2017**, *330*, 1334−1341.

(19) Zheng, J.; Zhou, W.; Ma, Y.; Cao, W.; Wang, C.; Guo, L. "Facet-Dependent NiS_2 Polyhedrons on Counter Electrodes for Dye-Sensitized Solar Cells". *Chem. Commun.* **2015**, *51*, 12863−12866.

(20) Aliabadi, M. "Controllable Synthesis of $NiSe_2$ Nanostructures via Hydrothermal Process for Photocatalytic and Solar Cell Applications". *J. Inorg. Organomet. Polym.* **2017**, *27*, 73−79.

(21) Lu, Z. W.; Klein, B. M.; Singh, D. J. "Electronic Structure of Heazlewoodite Ni_3S_2". *Phys. Rev. B: Condens. Matter Mater. Phys.* **1996**, *54*, 13542−13545.

(22) Wang, J.-H.; Cheng, Z.; Brédas, J.-L.; Liu, M. "Electronic and Vibrational Properties of Nickel Sulfides from First Principles". *J. Chem. Phys.* **2007**, *127*, 214705.

(23) Koutti, L.; Hugel, J. "Origin of the Bandgap in the Antiferromagnetic NiS". *J. Phys.: Condens. Matter* **1999**, *11*, 1979−1988.

(24) Molla, A.; Sahu, M.; Hussain, S. "Synthesis of Tunable Band Gap Semiconductor Nickel Sulphide Nanoparticles: Rapid and Round the Clock Degradation of Organic Dyes". *Sci. Rep.* **2016**, *6*, 26034.

(25) Xu, K.; Ding, H.; Lv, H.; Tao, S.; Chen, P.; Wu, X.; Chu, W.; Wu, C.; Xie, Y. "Understanding Structure-Dependent Catalytic Performance of Nickel Selenides for Electrochemical Water Oxidation". *ACS Catal.* **2017**, *7*, 310−315.
(26) Yu, B.; Hu, Y.; Qi, F.; Wang, X.; Zheng, B.; Liu, K.; Zhang, W.; Li, Y.; Chen, Y. "Nanocrystalline $Ni_{0.85}Se$ as Efficient Non-noble-metal Electrocatalyst for Hydrogen Evolution Reaction". *Electrochim. Acta* **2017**, *242*, 25−30.
(27) Srinivas, K.; Chen, Y.; Wang, B.; Yu, B.; Wang, X.; Hu, Y.; Lu, Y.; Li, W.; Zhang, W.; Yang, D. "Metal−Organic Framework-Derived NiS/Fe_3O_4 Heterostructure-Decorated Carbon Nanotubes as Highly Efficient and Durable Electrocatalysts for Oxygen Evolution Reaction". *ACS Appl. Mater. Interfaces* **2020**, *12*, 31552−31563.
(28) Srinivas, K.; Chen, Y.; Wang, X.; Wang, B.; Karpuraranjith, M.; Wang, W.; Su, Z.; Zhang, W.; Yang, D. "Constructing Ni/NiS Heteronanoparticle-Embedded Metal−Organic Framework-Derived Nanosheets for Enhanced Water-Splitting Catalysis". *ACS Sustainable Chem. Eng.* **2021**, *9*, 1920−1931.
(29) Wei, C.; Cheng, C.; Cheng, Y.; Wang, Y.; Xu, Y.; Du, W.; Pang, H. "Comparison of NiS_2 and α-NiS Hollow Spheres for Supercapacitors, Non-Enzymatic Glucose Sensors and Water Treatment". *Dalton Trans.* **2015**, *44*, 17278−17285.
(30) Li, Q.; Wang, D.; Han, C.; Ma, X.; Lu, Q.; Xing, Z.; Yang, X. "Construction of Amorphous Interface in an Interwoven NiS/NiS_2 Structure for Enhanced Overall Water Splitting". *J. Mater. Chem. A* **2018**, *6*, 8233−8237.
(31) Luo, P.; Zhang, H.; Liu, L.; Zhang, Y.; Deng, J.; Xu, C.; Hu, N.; Wang, Y. "Targeted Synthesis of Unique Nickel Sulfide (NiS, NiS_2) Microarchitectures and the Applications for the Enhanced Water Splitting System". *ACS Appl. Mater. Interfaces* **2017**, *9*, 2500−2508.
(32) Yuan, B.; Luan, W.; Tu, S.-t. "One-Step Solvothermal Synthesis of Nickel Selenide Series: Composition and Morphology Control". *CrystEngComm* **2012**, *14*, 2145−2151.
(33) Zhai, L.; Lo, T. W. B.; Xu, Z.-L.; Potter, J.; Mo, J.; Guo, X.; Tang, C. C.; Tsang, S. C. E. T.; Lau, S. P. "In Situ Phase Transformation on Nickel-Based Selenides for Enhanced Hydrogen Evolution Reaction in Alkaline Medium". *ACS Energy Lett.* **2020**, *5*, 2483−2491.
(34) Yin, M.; O'Brien, S. "Synthesis and Characterization of Nanostructured Nickel Diselenide $NiSe_2$ from the Decomposition of Nickel Acetate, $(CH_3CO_2)_2Ni$". *J. Nanomater.* **2014**, *2014*, 1−7.
(35) Hyde, B.; Okeeffe, M. "Marcasite and Pyrite (FeS_2)". *Aust. J. Chem.* **1996**, *49*, 867−872.
(36) Schmøkel, M. S.; Bjerg, L.; Cenedese, S.; Jorgensen, M. R. V.; Chen, Y.-S.; Overgaard, J.; Iversen, B. B. "Atomic Properties and Chemical Bonding in the Pyrite and Marcasite Polymorphs of FeS_2: A Combined Experimental and Theoretical Electron Density Study". *Chem. Sci.* **2014**, *5*, 1408−1421.
(37) Yi, M.; Wu, J.; Zheng, X.; Ming, X. "Structural Transition from Marcasite to Pyrite Phase in FeS_2 Under High Pressure: A First-Principles Study". *Eur. Phys. J. B* **2020**, *93*, 179.
(38) Lennie, A. R.; Vaughan, D. J. "Kinetics of the Marcasite-Pyrite Transformation: An Infrared Spectroscopic Study". *Am. Mineral.* **1992**, *77*, 1166−1171.
(39) Gudelli, V. K.; Kanchana, V.; Appalakondaiah, S.; Vaitheeswaran, G.; Valsakumar, M. C. "Phase Stability and Thermoelectric Properties of the Mineral FeS_2: An Ab Initio Study". *J. Phys. Chem. C* **2013**, *117*, 21120−21131.
(40) Yao, X.; Xia, F.; Deditius, A. P.; Brugger, J.; Etschmann, B. E.; Pearce, M. A.; Pring, A. "The Mechanism and Kinetics of the Transformation from Marcasite to Pyrite: In Situ and Ex Situ Experiments and Geological Implications". *Contrib. Mineral. Petrol.* **2020**, *175*, 27.
(41) Miao, N.-X.; Lei, Y.-X.; Zhou, J.-P.; Hassan, Q. U. "Theoretical and Experimental Researches on NiS_2 Nanocubes with Uniform Reactive Exposure Facets". *Mater. Chem. Phys.* **2018**, *207*, 194−202.
(42) Han, Z.-H.; Yu, S.-H.; Li, Y.-P.; Zhao, H.-Q.; Li, F.-Q.; Xie, Y.; Qian, Y.-T. "Convenient Solvothermal Synthesis and Phase Control of Nickel Selenides with Different Morphologies". *Chem. Mater.* **1999**, *11*, 2302−2304.
(43) Roffey, A.; Hollingsworth, N.; Islam, H. U.; Mercy, M.; Sankar, G.; Catlow, R.; Hogarth, G.; Leeuw, N. H. "Phase Control During the Synthesis of Nickel Sulfide Nanoparticles from Dithiocarbamate Precursors". *Nanoscale* **2016**, *8*, 11067−11075.
(44) Yin, P.; Zhang, Z.; Zhou, C.; Sun, Y.; Han, X.; Deng, C.; Sun, L. "Facile Synthesis of Flake-like Nickel Disulfide Nanocrystallites". *Mater. Sci. Semicond. Process.* **2014**, *26*, 404−409.
(45) Moloto, N.; Moloto, M. J.; Coville, N. J.; Ray, S. S. "Optical and Structural Characterization of Nickel Selenide Nanoparticles Synthesized by Simple Methods". *J. Cryst. Growth* **2009**, *311*, 3924−3932.
(46) Dai, C.; Li, B.; Li, J.; Zhao, B.; Wu, R.; Ma, H.; Duan, X. "Controllable Synthesis of NiS and NiS_2 Nanoplates by Chemical Vapor Deposition". *Nano Res.* **2020**, *13*, 2506−2511.
(47) Zhang, G.; Wang, W.; Yu, Q.; Li, X. "Facile One-Pot Synthesis of PbSe and $NiSe_2$ Hollow Spheres: Kirkendall-Effect-Induced Growth and Related Properties". *Chem. Mater.* **2009**, *21*, 969−974.
(48) Ge, Z.-H.; Wei, K.; Nolas, G. S. "Synthesis and Low-Temperature Transport Properties of Polycrystalline $NiSe_2$". *Phys. Status Solidi A* **2013**, *210*, 2725−2728.
(49) *XRD Standard Patterns; Inorganic Crystal Structure Database*; Karlsruhe, Germany, 2021.
(50) Kullerud, G.; Yund, R. A. "The Ni-S System and Related Minerals". *J. Petrol.* **1962**, *3*, 126−175.
(51) Shombe, G. B.; Khan, M. D.; Zequine, C.; Zhao, C.; Gupta, R. K.; Revaprasadu, N. "Direct Solvent Free Synthesis of Bare α-NiS, β-NiS and α-β-NiS Composite as Excellent Electrocatalysts: Effect of Selfcapping on Supercapacitance and Overall Water Splitting Activity". *Sci. Rep.* **2020**, *10*, 3260.
(52) Bai, B.; Xuemei, H.; Pengpeng, W.; Weisheng, G. "Microwave Hydrothermal Synthesis and Characterizations of NiS Nano-Needle". *SPIE Proceedings, Second International Conference on Smart Materials and Nanotechnology in Engineering*, 2009; Vol 7493, p 749360.
(53) Shen, G.; Chen, D.; Tang, K.; An, C.; Yang, Q.; Qian, Y. "Phase-Controlled Synthesis and Characterization of Nickel Sulfides Nanorods". *J. Solid State Chem.* **2003**, *173*, 227−231.
(54) Zhang, X.; Scott, T.; Socha, T.; Nielsen, D.; Manno, M.; Johnson, M.; Yan, Y.; Losovyj, Y.; Dowben, P.; Aydil, E. S.; Leighton, C. "Phase Stability and Stoichiometry in Thin Film Iron Pyrite: Impact on Electronic Transport Properties". *ACS Appl. Mater. Interfaces* **2015**, *7*, 14130−14139.
(55) Moon, D. G.; Cho, A.; Park, J. H.; Ahn, S.; Kwon, H.; Cho, Y. S.; Ahn, S. "Iron Pyrite Thin Films Deposited via Non-vacuum Direct Coating of Iron-salt/Ethanol-based Precursor Solutions". *J. Mater. Chem. A* **2014**, *2*, 17779−17786.
(56) Thomson, J. W.; Nagashima, K.; Macdonald, P. M.; Ozin, G. A. "From Sulfur−Amine Solutions to Metal Sulfide Nanocrystals: Peering into the Oleylamine−Sulfur Black Box". *J. Am. Chem. Soc.* **2011**, *133*, 5036−5041.
(57) Frenette, L. C.; Krauss, T. D. "Unconvering Active Precursors in Colloidal Quantum Dot Synthesis". *Nat. Commun.* **2017**, *8*, 2082.
(58) Seefeld, S.; Limpinsel, M.; Liu, Y.; Farhi, N.; Weber, A.; Zhang, Y.; Berry, N.; Kwon, Y. J.; Perkins, C. L.; Hemminger, J. C.; Wu, R.; Law, M. "Iron Pyrite Thin Films Synthesized from an $Fe(acac)_3$ Ink". *J. Am. Chem. Soc.* **2013**, *135*, 4412−4424.
(59) Yang, T.; He, Y.; Liu, X.; Liu, X.; Peng, Q.; Li, N.; Liu, J. "Mapping Surface Morphology and Phase Evolution of Iron Sulfide Nanoparticles". *CrystEngComm* **2021**, *23*, 5645−5654.
(60) Parija, A.; Waetzig, G. R.; Andrews, J. L.; Banerjee, S. "Traversing Energy Landscapes Away from Equilibrium: Strategies for Accessing and Utilizing Metastable Phase Space". *J. Phys. Chem. C* **2018**, *122*, 25709−25728.
(61) Csonka, G. I.; Perdew, J. P.; Ruzsinszky, A.; Philipsen, P. H. T.; Lebégue, S.; Paier, J.; Vydrov, O. A.; Ángyán, J. G. "Assessing the Performance of Recent Density Functionals for Bulk Solids". *Phys. Rev. B: Condens. Matter Mater. Phys.* **2009**, *79*, 155107.
(62) Perdew, J. P.; Ruzsinszky, A.; Csonka, G. I.; Vydrov, O. A.; Scuseria, G. E.; Constantin, L. A.; Zout, X.; Burke, K. "Restoring the

https://doi.org/10.1021/acs.chemmater.1c03557
Chem. Mater. 2022, 34, 746−755

Density-Gradient Expansion for Exchange in Solids and Surfaces". *Phys. Rev. Lett.* **2008**, *100*, 136406.
(63) Francis, G. P.; Payne, M. C. "Finite Basis Set Correction to Total Energy Pseudopotential Calculations". *J. Phys.: Condens. Matter* **1990**, *2*, 4395−4404.
(64) Murnaghan, F. D. "The Compressibility of Media under Extreme Pressures". *Proc. Natl. Acad. Sci. U.S.A.* **1944**, *30*, 244−247.
(65) Birch, F. "Finite Elastic Strain of Cubic Crystals". *Phys. Rev.* **1947**, *71*, 809−824.
(66) Zhang, M.-Y.; Cui, Z.-H.; Jiang, H. "Relative Stability of FeS_2 Polymorphs with the Random Phase Approximation Approach". *J. Mater. Chem. A* **2018**, *6*, 6606−6616.
(67) Spagnoli, D.; Refson, K.; Wright, K.; Gale, J. D. "Density Functional Theory Study of the Relative Stability of the Iron Disulfide Polymorphs Pyrite and Marcasite". *Phys. Rev. B: Condens. Matter Mater. Phys.* **2010**, *81*, 094106-1−094106-9.
(68) Li, Y.; Chen, J.; Chen, Y.; Zhao, C.; Lee, M.-H.; Lin, T.-H. "DFT+U Study on the Electronic Structures and Optical Properties of Pyrite and Marcasite". *Comput. Mater. Sci.* **2018**, *150*, 346−352.
(69) Song, J.; Huang, Z.-F.; Pan, L.; Li, K.; Zhang, X.; Wang, L.; Zou, J.-J. "Review on Selective Hydrogenation of Nitroarene by Catalytic, Photocatalytic, and Electrocatalytic Reactions". *Appl. Catal., B* **2018**, *227*, 386−408.
(70) Daniels, C. L.; Liu, D.-J.; Adamson, M. A. S.; Knobeloch, M.; Vela, J. "Azo(xy) vs Aniline Selectivity in Catalytic Nitroarene Reduction by Intermetallics: Experiments and Simulations". *J. Phys. Chem. C* **2021**, *125*, 24440−24450.
(71) Jiang, N.; Tang, Q.; Sheng, M.; You, B.; Jiang, D.-e.; Sun, Y. "Nickel Sulfides for Electrocatalytic Hydrogen Evolution Under Alkaline Conditions: A Case Study of Crystalline NiS, NiS_2, and Ni_3S_2 Nanoparticles". *Catal. Sci. Technol.* **2016**, *6*, 1077−1084.
(72) Kresse, G.; Hafner, J. "Ab Initio Molecular Dynamics for Liquid Metals". *Phys. Rev. B: Condens. Matter Mater. Phys.* **1993**, *47*, 558−561.
(73) Kresse, G.; Hafner, J. "Ab Initio Molecular-Dynamics Simulation of the Liquid-Metal-Amorphous-Semiconductor Transition in Germanium". *Phys. Rev. B: Condens. Matter Mater. Phys.* **1994**, *49*, 14251−14269.
(74) Kresse, G.; Furthmüller, J. "Efficiency of Ab-Initio Total Energy Calculations for Metals and Semiconductors Using a Plane-Wave Basis Set". *Comput. Mater. Sci.* **1996**, *6*, 15−50.
(75) Kresse, G.; Furthmüller, J. "Efficient Iterative Schemes for Ab Initio Total-Energy Calculations Using a Plane-Wave Basis Set". *Phys. Rev. B: Condens. Matter Mater. Phys.* **1996**, *54*, 11169−11186.
(76) Kresse, G.; Joubert, D. "From Ultrasoft Pseudopotentials to the Projector Augmented-Wave Method". *Phys. Rev. B: Condens. Matter Mater. Phys.* **1999**, *59*, 1758−1775.
(77) Monkhorst, H. J.; Pack, J. D. "Special Points for Brillouin-Zone Integrations". *Phys. Rev. B: Solid State* **1976**, *13*, 5188−5192.
(78) Press, W. H.; Flannery, B. P.; Teukolsky, S. A.; Vetterling, W. T. *"Numerical Recipes in PASCAL"*; Cambridge University Press: Cambridge, 1989; pp 339−345.

https://doi.org/10.1021/acs.chemmater.1c03557
Chem. Mater. 2022, 34, 746−755